Influences of the Indian Summer Monsoon on Water Vapor and Ozone Concentrations in the UTLS as Simulated by Chemistry–Climate Models

MARKUS KUNZE,* PETER BRAESICKE,+ ULRIKE LANGEMATZ,* GABRIELE STILLER,# SLIMANE BEKKI,@ CHRISTOPH BRÜHL,& MARTYN CHIPPERFIELD,** MARTIN DAMERIS,++ ROLANDO GARCIA,## AND MARCO GIORGETTA@@

* *Institut für Meteorologie, Freie Universität Berlin, Berlin, Germany*
+ *NCAS-Climate-Chemistry, University of Cambridge, Cambridge, United Kingdom*
# *Forschungszentrum Karlsruhe, Institut für Meteorologie und Klimaforschung, Karlsruhe, Germany*
@ *LATMOS-IPSL, UVSQ, UPMC, CNRS/INSU, Paris, France*
& *Max-Planck-Institut für Chemie, Mainz, Germany*
** *University of Leeds, Leeds, United Kingdom*
++ *Deutsches Zentrum für Luft- und Raumfahrt, Institut für Physik der Atmosphäre, Oberpfaffenhofen, Germany*
National Center for Atmospheric Research, Boulder, Colorado
@@ *Max-Planck-Institut für Meteorologie, Hamburg, Germany*

(Manuscript received 8 June 2009, in final form 29 January 2010)

ABSTRACT

The representation of the Indian summer monsoon (ISM) circulation in some current chemistry–climate models (CCMs) is assessed. The main assessment focuses on the anticyclone that forms in the upper troposphere and lower stratosphere and the related changes in water vapor and ozone during July and August for the recent past. The synoptic structures are described and CCMs and reanalysis models are compared. Multiannual means and weak versus strong monsoon cases as classified by the Monsoon–Hadley index (MHI) are discussed. The authors find that current CCMs capture the average synoptic structure of the ISM anticyclone well as compared to the 40-yr ECMWF Re-Analysis (ERA-40) and NCEP–NCAR reanalyses. The associated impact on water vapor and ozone in the upper troposphere and lower stratosphere as observed with the Michelson Interferometer for Passive Atmospheric Sounding (MIPAS) on *Envisat* is captured by most models to some degree. The similarities for the strong versus weak monsoon cases are limited, and even for present-day conditions the models do not agree well for extreme events. Nevertheless, some features are present in the reanalyses and more than one CCM, for example, ozone increases at 380 K eastward of the ISM. With the database available for this study, future changes of the ISM are hard to assess. The modeled monsoon activity index used here shows slight weakening of the ISM circulation in a future climate, and some of the modeled water vapor increase seems to be contained in the anticyclone at 360 K and sometimes above. The authors conclude that current CCMs capture the average large-scale synoptic structure of the ISM well during July and August, but large differences for the interannual variability make assessments of likely future changes of the ISM highly uncertain.

1. Introduction

The Indian summer monsoon (ISM) is a major source of interannual variability in the Northern Hemisphere (Annamalai et al. 1999). It is a significant moisture source for the upper troposphere outside the deep tropics with a potential to moisten the lower stratosphere (Dethof et al. 1999). The current generation of Intergovernmental Panel on Climate Change (IPCC) coupled ocean–atmosphere climate models shows variable skill in capturing aspects of the monsoon variability (e.g., Kripalani et al. 2007, and references therein). Here we will assess the ability of chemistry–climate models (CCMs), driven with observed monthly mean sea surface temperatures (SSTs), to capture the large-scale monsoon circulation and its impact on trace gas distributions, in particular water vapor and ozone. Three questions form the main focus: Are the models capable of capturing the mean state of the upper troposphere/lower stratosphere (UTLS) ISM anticyclone?

Corresponding author address: Markus Kunze, Institut für Meteorologie, Freie Universität Berlin, Carl-Heinrich-Becker-Weg 6-10, 12165 Berlin, Germany.
E-mail: markus.kunze@met.fu-berlin.de

DOI: 10.1175/2010JCLI3280.1

Are the models able to capture the observed interannual variability of the ISM anticyclone? Do the models predict changes in the ISM in the future?

The ISM is a seasonal and regional feature, occurring between June and September over the Indian subcontinent. It is so large a feature that it determines to some extent the annual and zonal mean state of the atmosphere in low to middle latitudes in the Northern Hemisphere. Capturing such a major mode of variability correctly is an important test for the performance of CCMs, and deficits in representing the ISM will affect highly averaged quantities used in policy assessments (e.g., WMO 2007). The ISM is not only a purely dynamical phenomenon affecting winds (triggered by land–sea temperature contrasts), it is also important for trace gas distributions in the upper troposphere and lower stratosphere, potentially lifting pollution and water vapor from the troposphere into the lowermost stratosphere on short time scales.

The obvious trace gas immediately affected by a monsoon is water vapor, which is transported inland in the lower troposphere but is also transported upward and has a distinct distribution in the upper troposphere during the lifetime of the ISM anticyclone. Moistening or drying of the lowermost stratosphere due to changes in the ISM would have climate relevant consequences for the radiative balance of the atmosphere (Shine and Forster 1999). Nonetheless, aspects of its temporal evolution in the UTLS and how it is linked to ISM variability remain unclear (e.g., Oltmans et al. 2000; Rosenlof et al. 2001; Fueglistaler and Haynes 2005; Randel et al. 2006; Scherer et al. 2008).

Chen (1995) diagnosed isentropic exchange between the troposphere and the stratosphere at 340 K and above during the active phase of the ISM. In addition, a model study by Dethof et al. (1999) highlighted the potential of the ISM to moisten the extratropical upper tropopause. Subsequently lower stratospheric water vapor could increase. In another model study, Bannister et al. (2004) showed that the largest contribution to the moist phase of the so-called stratospheric tape recorder (Mote et al. 1996) during June, July, and August could be attributed to the ISM. James et al. (2008) analyzed backward trajectories to identify the pathways of air parcels contributing to the ISM water vapor maximum at 100 hPa. By convection over the Bay of Bengal and the South China Sea moist air is transported into the tropical tropopause layer (TTL). The air parcels are then transported through the TTL by the ISM anticyclonic circulation toward northwest India, where they are finally dehydrated, avoiding bypassing the coldest point of the TTL (James et al. 2008). Dessler and Sherwood (2004) used a simple model to show that convection can lead to an increase of extratropical water vapor around the 380-K isentropic level of 40%. The 380-K level in the extratropics is in the lower stratosphere and is close to the tropopause in tropical latitudes. Gettelman et al. (2004) analyzed data from a chemistry transport model and found that the ISM contributes 75% of the total net upward water vapor flux in the tropics at tropopause levels from July to September. Levine et al. (2008) pointed out that no clear monsoon signal is apparent in transport studies from the tropical tropopause layer into the lowermost stratosphere. The large-scale meridional winds as associated with the ISM are important in determining the seasonality and hemispheric preference for transport from the TTL into the lowermost stratosphere.

Another important trace gas affected by the ISM is ozone. For the policy-relevant monitoring of the Montreal protocol and its amendments, it is necessary to evaluate our ability to detect ozone recovery due to changes in the halogen loading (WMO 2007). Attribution of ozone changes requires an understanding of interannual ISM variability. Like water vapor, ozone in the UTLS is an important radiatively active species and partly determines vertical temperature gradients (Shine and Forster 1999).

Recent satellite observations have helped to characterize the ISM impact on trace gas distributions over the Indian subcontinent in more detail. Randel and Park (2006) analyzed upper tropospheric water vapor and ozone concentrations from the Atmospheric Infrared Sounder (AIRS) and found a strong link to convection. Park et al. (2007) analyzed Microwave Limb Sounder (MLS) data of carbon monoxide, water vapor, ozone, and temperature from *Aura* and identified at the eastern edge of the monsoon anticyclone rising motion, potentially transporting trace gases from the region of convective outflow (~12 km) to the level of the tropopause. Michelson Interferometer for Passive Atmospheric Sounding (MIPAS) CO observations also imply an important role of the ISM in upward transport (Funke et al. 2009).

Here, we will study the ability of current CCMs to capture the climatology of the ISM and its impact on water vapor and ozone. We will focus on model runs covering the recent past (CCMVal-1 REF1) (Eyring et al. 2006), assessing their mean ISM, their ISM-related transport regimes as manifested in water vapor and ozone, and their interannual variability of the ISM and its impact on tracers in comparison with reanalysis output.

For available future projections (CCMVal-1 REF2) (Eyring et al. 2007) of two CCMs, we will present an initial study of the changes in UTLS water vapor and ozone concentrations related to the monsoon circulations in a changing climate.

The plan of the paper is as follows. In section 2 we introduce our diagnostic strategy and data, while section 3

TABLE 1. Chemistry–climate models used.

Model	Horizontal resolution	Number of levels/upper boundary	Underlying GCM	Group and location
E39C	3.75° × 3.75°(T30)	39/10 hPa	ECHAM4.L39 (DLR)	DLR, Oberpfaffenhofen, Germany
LMDZrepro	2.5° × 3.75°	50/0.07 hPa	LMDz4	L'Institut Pierre-Simon Laplace (IPSL), Paris, France
MAECHAM4CHEM	3.75° × 3.75°(T30)	39/0.01 hPa	MAECHAM4	MPI-C, Mainz, MPI-M, Hamburg, Germany
UMSLIMCAT	2.5° × 3.75°	64/0.01 hPa	Unified Model	University of Leeds, Leeds, United Kingdom
WACCM(v3)	4.5° × 5°	66/0.0000045 hPa	Community Atmosphere Model (CAM)	NCAR, Boulder, Colorado

discusses the synoptic characteristics of observed and modeled dynamical monsoon features in the UTLS. In section 4 we show the effect of the ISM circulation on water vapor and ozone concentrations in the UTLS and in section 5 describe features of interannual monsoon variability in water vapor and ozone. Section 6 provides first-order estimates of future monsoon changes and characterizes potential impacts on water vapor and ozone. A summary and an outlook are provided in section 7.

2. Methodology, models, and data

We focus on the evaluation of the fully developed Indian summer monsoon (ISM) during July and August using monthly mean wind, geopotential height, and temperature data from a set of CCMVal-1 REF1 integrations, as summarized in Eyring et al. (2006) and used in the World Meteorological Organization–United Nations Environment Programme report ''Scientific Assessment of Ozone Depletion: 2006'' (WMO 2007).

The mean synoptic ISM structures in the upper troposphere and lower stratosphere are analyzed. Geopotential heights and streamlines, averaged over 1980–99, are evaluated and compared to 40-yr European Centre for Medium-Range Weather Forecasts Re-Analysis (ERA-40) (Uppala et al. 2005) and National Centers for Environmental Prediction (NCEP)–National Center for Atmospheric Research (NCAR) reanalysis (Kalnay et al. 1996; Kistler et al. 2001) output.

Similarly, the averaged large-scale features in the water vapor and ozone distributions associated with the ISM, which are derived from the CCM simulations and ERA-40 data, are compared. NCEP–NCAR does not provide water vapor data in the UTLS and does not provide any ozone data. The ERA-40 water vapor and ozone are only weakly constrained by observations (Oikonomou and O'Neill 2006). In contrast to the temperature and wind data, the ERA-40 water vapor and ozone data should be considered model output rather than observations. Therefore, ozone and water vapor are investigated using MIPAS satellite data of water vapor (Milz et al. 2009; von Clarmann et al. 2009) and ozone (Steck et al. 2007; von Clarmann et al. 2009). MIPAS measures water vapor and ozone, among numerous other species, as a limb emission midinfrared sounder with high spectral resolution from a sun-synchronous polar orbit at about 800-km altitude. It covers the atmosphere from 70 km to cloud top by scanning from top to bottom with a step width of 1.5 km (upper troposphere/lower stratosphere, since 2005) to 8 km (mesosphere, before 2005). Data are recorded every 400 km along the orbit, with 14.4 orbits per day, providing one profile per day roughly every 4° latitude and 12.5° longitude. Cloud contamination reduces the achievable coverage. The atmospheric distributions

TABLE 2. Main specifications of CCMVal-1 REF1 simulations.

Model	Quasi-biennial oscillation (QBO)	Volcanoes	Solar cycle	SSTs	Greenhouse gas (GHG)	Halogenes
MAECHAM4CHEM	Assim.	Yes	Yes	Hadley Centre Global Sea Ice and Sea Surface Temperature, v1 (HadISST1)	IPCC A2	WMO (2003)
E39C	Assim.	Yes	Yes	HadISST1	IPCC A2	WMO (2003)
WACCM(v3)	No	Yes	Yes	J. Hurrell (2005, personal communication)	WMO (2003)	WMO (2003)
UMSLIMCAT	Internal	Yes	No	Atmospheric Model Intercomparison Project (AMIP) II	IPCC A2	WMO (2003)
LMDZrepro	No	Yes	No	AMIP II	WMO (2003)	WMO (2003)

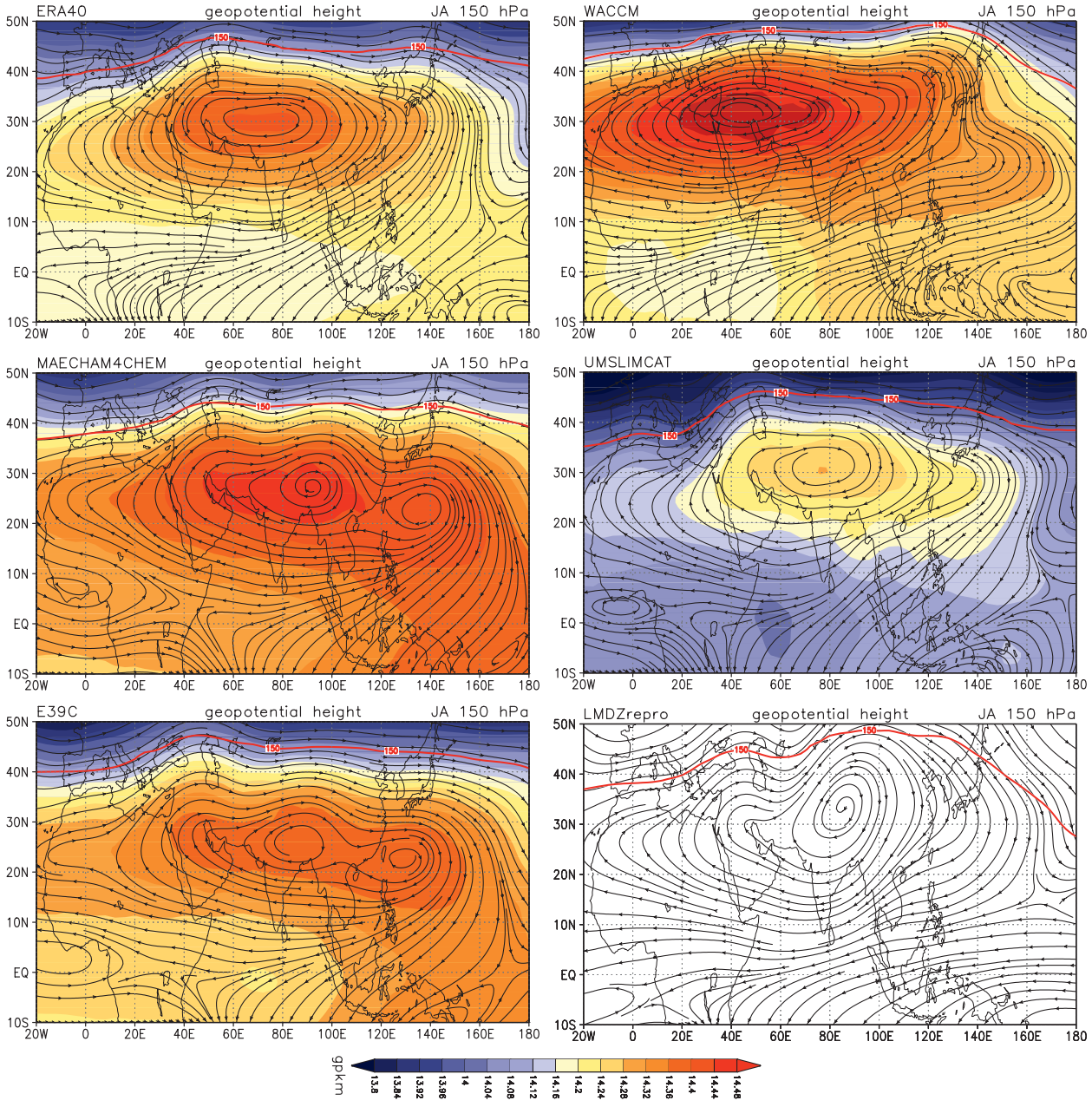

FIG. 1. Long-term monthly mean (20 yr; 1980–99) for July/August of the 150-hPa geopotential height for 10°S–50°N, 20°W–180°, shaded in gpkm. Overlaid as streamlines are the horizontal wind components. The red line indicates the lapse rate tropopause.

of water vapor and ozone used in this study were retrieved with the MIPAS level-2 data processor at the Institut für Meteorologie und Klimaforschung–Instituto de Astrofísica de Andalucía (von Clarmann et al. 2003) from observations of 57 days overall during July and August 2003, 2005, 2006, and 2007. The precision, accuracy, and vertical resolution of single profiles in the relevant altitude range of water vapor (ozone) is 5%–6%, 8%–17%, and 2.3–3.3 km (3.8–12.6%, 9.6–17.0%, 2.4–2.9 km), respectively (von Clarmann et al. 2009).

The selection of characteristic vertical levels to use in such a comparison is slightly arbitrary and is guided by available data and previous work. We will focus on the 150-hPa pressure level and the 380-K isentropic level, which in the tropics are fairly parallel, with the 150-hPa pressure level being slightly lower in altitude compared to 380 K. The intersection of pressure and isentropic levels in conjunction with the configuration of streamlines might be indicative of isentropic transport and troposphere–stratosphere exchange. The approach here

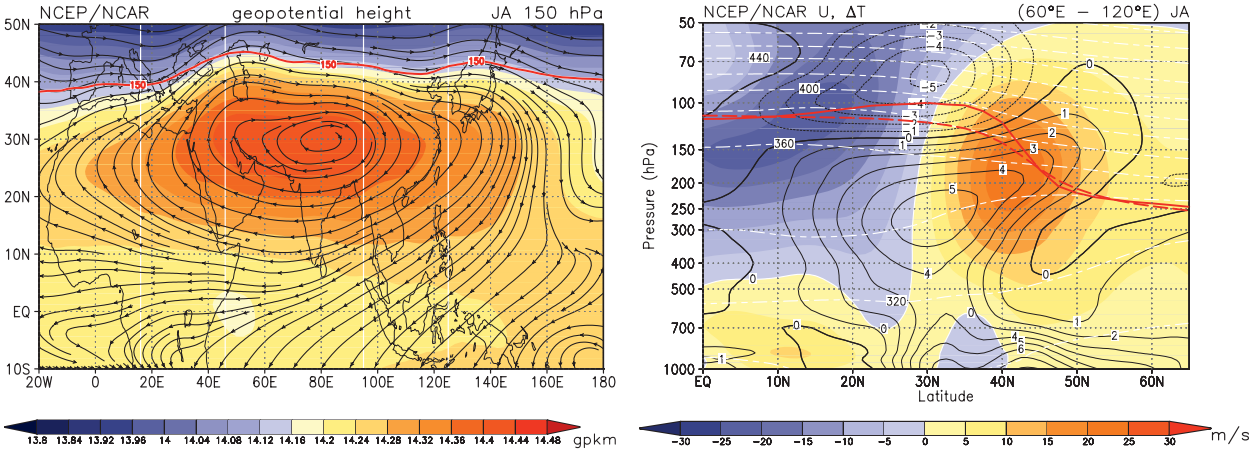

FIG. 2. (left) As in Fig. 1 but for the NCEP–NCAR reanalysis. The vertical white lines mark the sections used in Fig. 3. (right) Latitude–height sections between 1000 and 50 hPa from the equator to 65°N for the July/August long-term mean (20 yr) zonal velocity averaged between 60° and 120°E: shading interval 5 m s^{-1}. Displayed as contours in black are the temperature anomalies of the respective latitude section relative to the zonal average. The white dashed contours indicate the isentropic surfaces (contour interval 20 K). Displayed in red is the lapse rate tropopause: zonal mean (dashed) averaged between 60° and 120°E (solid). Data are from the NCEP–NCAR reanalysis.

is limited by the use of monthly mean data, which allows only the representation of a quasi-stationary mean state and cannot take into account temporal variability on shorter time scales that is important for the net transport of air. The selected horizontal maps will be supported by latitude–height cross sections at different longitudes to reveal the three-dimensional structure of the ISM circulation.

We selected the Monsoon–Hadley index (MHI) (Goswami et al. 1999) as a suitable monthly mean monsoon index to describe interannual variability. The MHI index is strongly correlated with the classical All-India Monsoon Rainfall Index (AIR) (Mooley and Parthasarathy 1984), which is based on the amount of precipitation falling during the months from June to September at stations on the Indian subcontinent. The MHI is dynamically defined and is, therefore, a measure for the strength of the ISM circulation. It is based on the anomalous meridional wind shear averaged over the region 10°–30°N, 70°–110°E. The deviation of the meridional wind v_i from the long-term area mean v_{ltm} is calculated at 850 and 200 hPa for every single July–August season i:

$$\mathrm{MHI}_i = [v_{\mathrm{ltm}}(850) - v_i(850)] - [v_{\mathrm{ltm}}(200) - v_i(200)].$$

Large positive values of the MHI indicate a strong northward-directed (southward-directed) meridional wind at 850 hPa (200 hPa). Negative MHI correspond to weak ISM cases. Using this monsoon index, we will stratify the data (CCMs and ERA-40) and form composites for strong and weak monsoon cases. We assess how the interannual variability, in particular amplitude and changes in spatial distribution of the ISM anticyclone, is captured in CCMs compared to reanalysis systems.

The following models are used in this assessment: MAECHAM4CHEM (Steil et al. 2003; Manzini et al. 2003), E39C (Dameris et al. 2005), WACCM (Garcia et al. 2007), UMSLIMCAT (Tian and Chipperfield 2005), and LMDZrepro (Jourdain et al. 2008) (see summary Table 1). Even though all models are global CCMs, they differ substantially in vertical and horizontal resolution, vertical domain, complexity of chemistry, and tracer transport. The setups of the model simulations used here are summarized in Table 2. Not all models have used the CCMVal-1 recommended REF1 setup in all details. Therefore, it might be very difficult to identify the causes of the differences diagnosed between the model simulations. Nevertheless, it is important to highlight those differences because they may be regarded as representative of the model uncertainties. Their estimation is crucial for assessment processes such as WMO (2007).

Using climate projections (Eyring et al. 2007) we will assess how future changes in the ISM project on water vapor and ozone changes. In conjunction with the earlier composite assessment for present-day climate, we will attempt to assess the likelihood of higher/lower water vapor and ozone values in the lowermost extratropical stratosphere and provide simple confidence measures for modeled future water vapor and ozone changes.

3. Synoptic description of climatological monsoon

The synoptic structure of the lower tropospheric ISM cyclone and the upper tropospheric ISM anticyclone has been well described in the past (Annamalai et al. 1999).

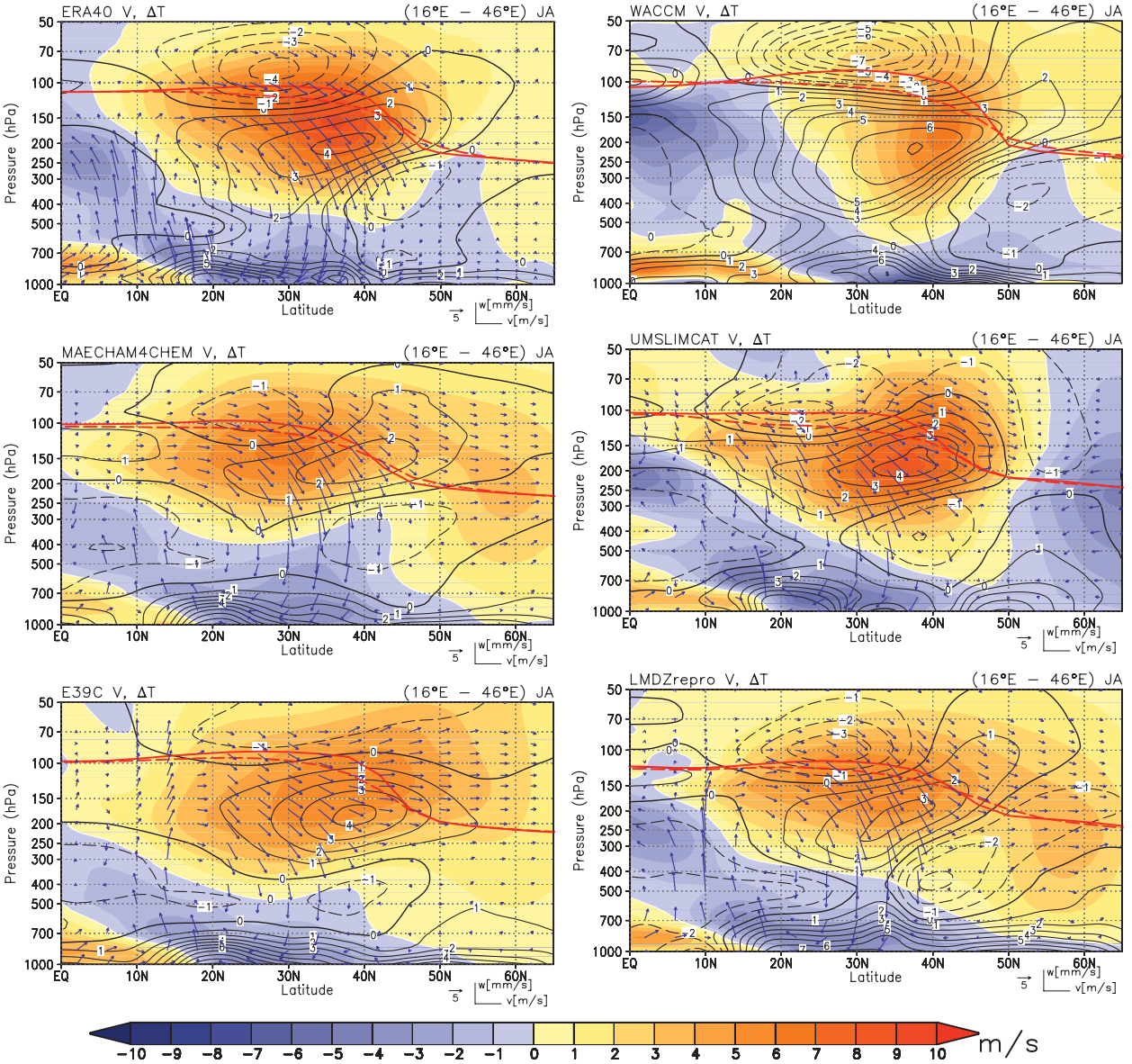

FIG. 3. Latitude–height sections between 1000 and 50 hPa from the equator to 65°N for the July/August long-term mean (20 yr) meridional velocity averaged over (left page) 16°–46°E and (right page) 95°–125°E; shading interval is 1 m s^{-1}. Displayed as contours in black are the temperature anomalies of the respective latitude sections relative to the zonal average. The tropopause height is displayed in red. The blue arrows denote the meridional (in m s^{-1}) and vertical velocity (in mm s^{-1}).

Early during Northern Hemisphere summer a large cyclone with its center over Pakistan develops in the lower troposphere. With increasing height the ISM cyclone in the lower troposphere transitions into an anticyclone in the UTLS.

Figure 1 shows the mean geopotential height and horizontal wind fields as represented by streamlines during July–August at the 150-hPa level for ERA-40 (top) and participating CCMs. The ISM anticyclone is captured by all models but varies considerably in strength, extent, and position. Note that the position of the ISM anticyclone affects further analyses because quantities are averaged for specific regions following earlier work (Dunkerton 1995). Area extent as measured by the 14.28 gpkm isoline is also highly variable. MAECHAM4CHEM, E39C, and WACCM all show much larger anticyclones than observed, whereas UMSLIMCAT calculates a much smaller anticyclone. The strongest (in terms of streamline density) circulation is modeled in WACCM, which also shows a marked displacement of the center of the anticyclone to the west with respect to the ERA-40 reanalysis. LMDZrepro did not provide geopotential

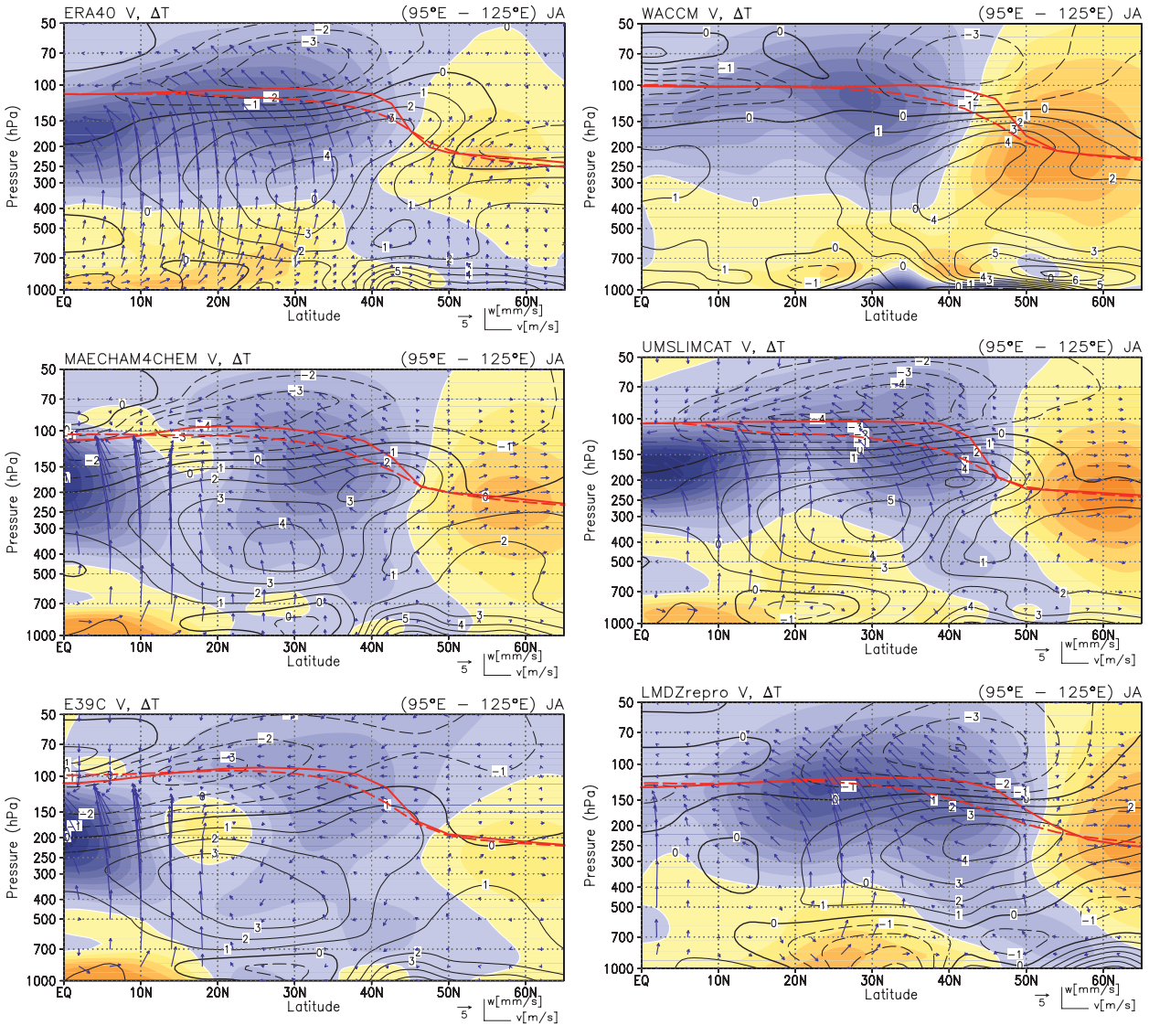

FIG. 3. (*Continued*)

height, but the streamlines indicate a strong, northward-displaced ISM anticyclone. It is interesting to note that MAECHAM4CHEM and E39C have been derived from the same parent general circulation model but have diverged in their development (transport scheme and vertical grid; E39C has 39 levels up to 10 hPa whereas MAECHAM4CHEM has 39 levels up to 0.01 hPa). Their ISM anticyclones are similar in structure but differ in strength, with MAECHAM4CHEM displaying the stronger circulation. Figure 2 (left) confirms the spatial distribution of the ISM anticyclone at 150 hPa from NCEP–NCAR reanalysis but suggests a slightly stronger circulation compared to ERA-40. Nevertheless, the difference between NCEP–NCAR and ERA-40 is much smaller than the differences revealed between CCMs and ERA-40 in Fig. 1.

To understand better the vertical ISM structure, we will analyze the western and eastern boundaries of the anticyclone. Figure 3 shows the meridional wind component (shaded) averaged zonally over (left) 16°–46°E and (right) 95°–125°E. Arrows indicate the vertical and meridional wind. Climatologically at 150 hPa these are the regions of prevailing northward (southward) meridional winds on the western (eastern) side of the ISM anticyclone.

The corresponding temperature anomalies relative to the zonal mean are shown as black contour lines (dashed

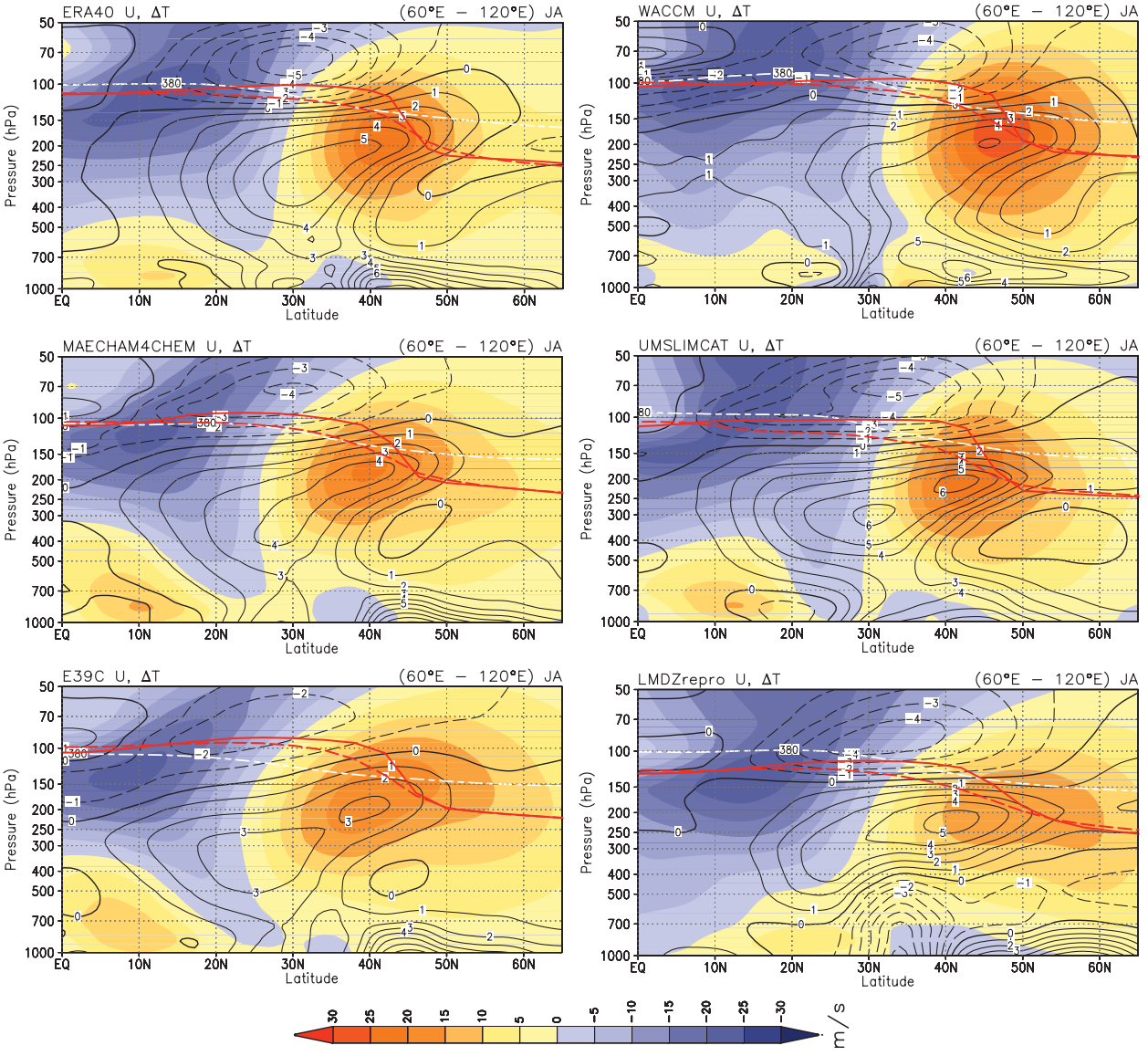

FIG. 4. As in Fig. 3 but averaged between 60° and 120°E for the zonal velocity and the 380-K potential temperature contour (dashed white): shading interval 5 m s^{-1}. Displayed in red is the lapse rate tropopause: zonal mean (dashed) averaged between 60° and 120°E (solid).

for negative values). The averaged lapse rate tropopause is indicated by a solid red line. The strongest northward-directed meridional velocities on the west side of the ISM anticyclone occur at 150 hPa between 30° and 45°N with values of 9 m s^{-1} in ERA-40 (top).

According to ERA-40, in the upper troposphere around 150 hPa on the western side of the monsoon anticyclone (Fig. 3, left) the northward-directed convergent meridional motion coincides with a downward-directed vertical velocity, whereas on the eastern side (Fig. 3, right) the divergent southward flow coincides with an upward vertical velocity. The southward meridional wind exceeds 7 m s^{-1} in ERA-40. In both areas a characteristic monsoon temperature pattern can be identified with positive anomalies in the troposphere and negative anomalies in the UTLS region. Dunkerton (1995) noted that the largest northward flow at the west side of the ISM anticyclone coincides with an acceleration of the zonal wind. Therefore, we analyze in Fig. 4 the zonally averaged zonal wind component (shaded), the temperature anomalies (black contours), the 380-K potential temperature contour (dashed white), and the tropopause temperature (solid red) averaged for a section from 60° to 120°E. The anomalies are calculated with respect to the zonal average (adapted from Randel and Park 2006, their Fig. 2).

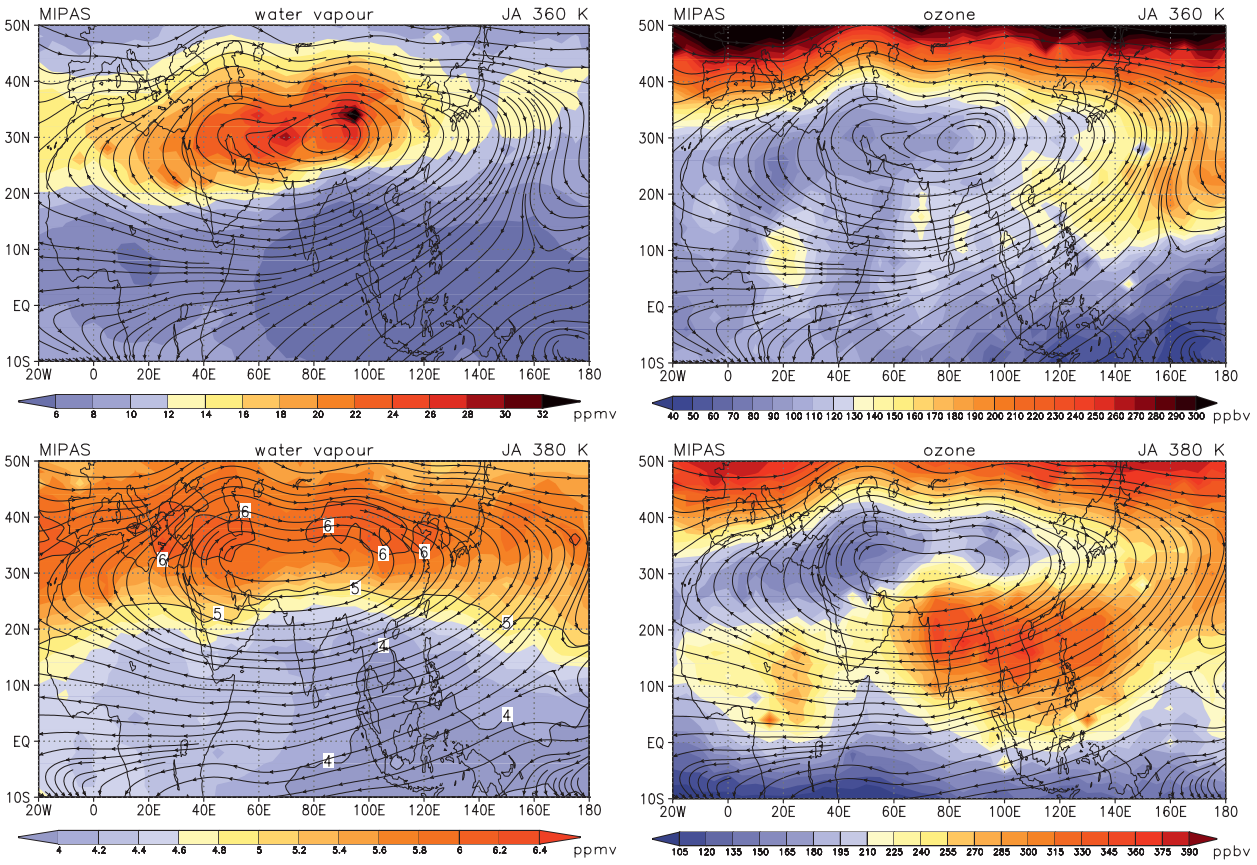

FIG. 5. MIPAS data (4 yr) for July–August at (top) 360 K and (bottom) 380 K for the region 10°S–50°N, 20°W–180°: (left) water vapor in ppmv, shaded with an interval of 2 (0.2) ppmv; (right) ozone in ppbv, shaded with an interval of 10 (15) ppbv at 360 (380) K. Overlaid as streamlines are the horizontal wind components of ECMWF analyses.

As analyzed by Randel and Park (2006) for July–August 2003 from NCEP–NCAR data, the structure of the climatological means derived from NCEP–NCAR (Fig. 2, right) and ERA-40 data is very similar. A well-developed westerly (eastward) jet is apparent. The westerly jet has a wind speed near 29 m s^{-1} in both reanalyses and is located near 40°N with its center between 200 and 150 hPa slightly below and equatorward of the downwardsloping tropical to subtropical tropopause averaged over this region. The center of the easterly jet is located near the tropopause (between 150 and 100 hPa) at 10°N. Due to latent heat release during the monsoon there is a positive temperature anomaly reaching from the troposphere in low latitudes to the lower stratosphere in high latitudes with a maximum of more than 5 K near 250 hPa at about 30°N. In the UTLS region the monsoon circulation induces the opposite temperature signal, peaking near 30°N above the tropopause at 80 hPa. A strong negative temperature anomaly is found in the center of the anticyclone, just above the tropopause, exceeding −5 K (see Fig. 4, top). Figure 2 (right) confirms the vertical thermal and dynamical structure diagnosed from ERA-40. As before, the difference between NCEP–NCAR and ERA-40 is much smaller than the differences revealed between CCMs and ERA-40 in Fig. 4.

The gross features of the ISM found in ERA-40 are apparent in all CCMs, but significant differences exist. Note that the ISM shows natural interannual variability and that the CCMs are only constrained with SSTs and sea ice coverage at the surface. Despite this constraint, the models still have a considerable degree of freedom to simulate weather and climate that is different from the observed weather and climate during the years from 1980 to 1999. Nevertheless, a couple of differences might be indicative of model deficiencies. The models of the ECHAM family have a maximum meridional velocity that is less pronounced than in the reanalyses and is slightly shifted toward 30°N. On the east side of the ISM anticyclone southward-directed meridional velocities with maxima around the subtropical tropopause are apparent (Fig. 3, right), but the modeled amplitude is highly variable. Toward the equator a second region with southward

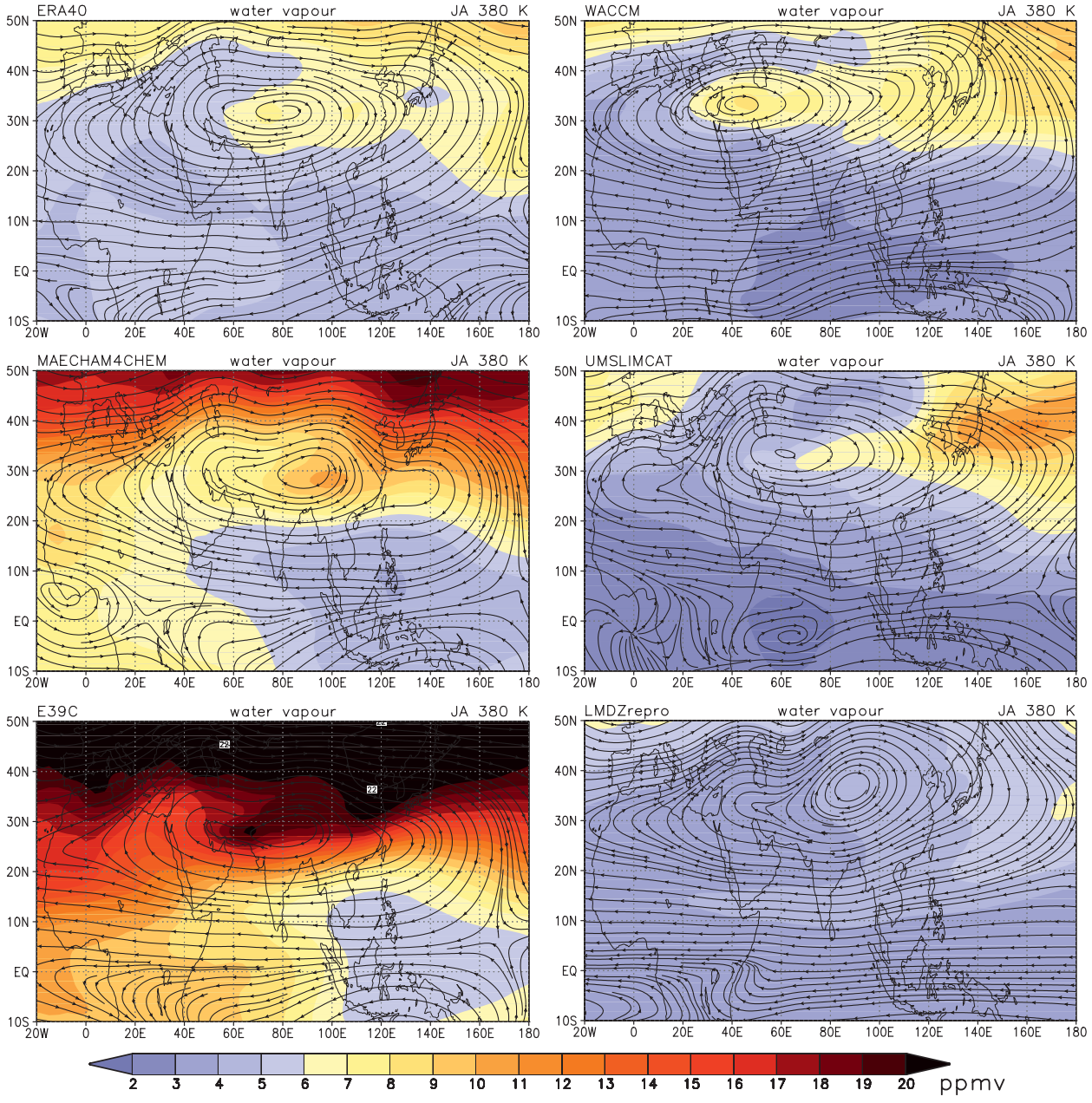

FIG. 6. Long-term monthly mean (20 yr) for July–August at 380 K for the region 10°S–50°N, 20°W–180°. (left page): water vapor (ppmv), shaded with an interval of 2 ppmv; (right page) ozone (ppbv), shaded with an interval of 15 ppbv. Overlaid as streamlines are the horizontal wind components.

meridional velocities emerges as part of the southern Hadley cell and is captured in all models apart from LMDZrepro, although only weakly in WACCM. This can be explained by the westward shift of the ISM anticyclone in the WACCM REF1 simulation; thus, using fixed regions for the sectional averages we do not fully capture the southern Hadley cell. This upper equatorial branch of the southern Hadley circulation can also be found very weakly and slightly lower in ERA-40 and to a variable extent in the CCMs. Note that this statement relies on the position of the ISM anticyclone and the areas defined to average over. The width of the modeled tropical tropopause break is variable. The tropopause break in ERA-40 is located around 40°N and coincides with the strongest meridional motions in both directions. Quasi-stationary cross-tropopause flow is evident in this region and stratosphere–troposphere exchange is likely to occur.

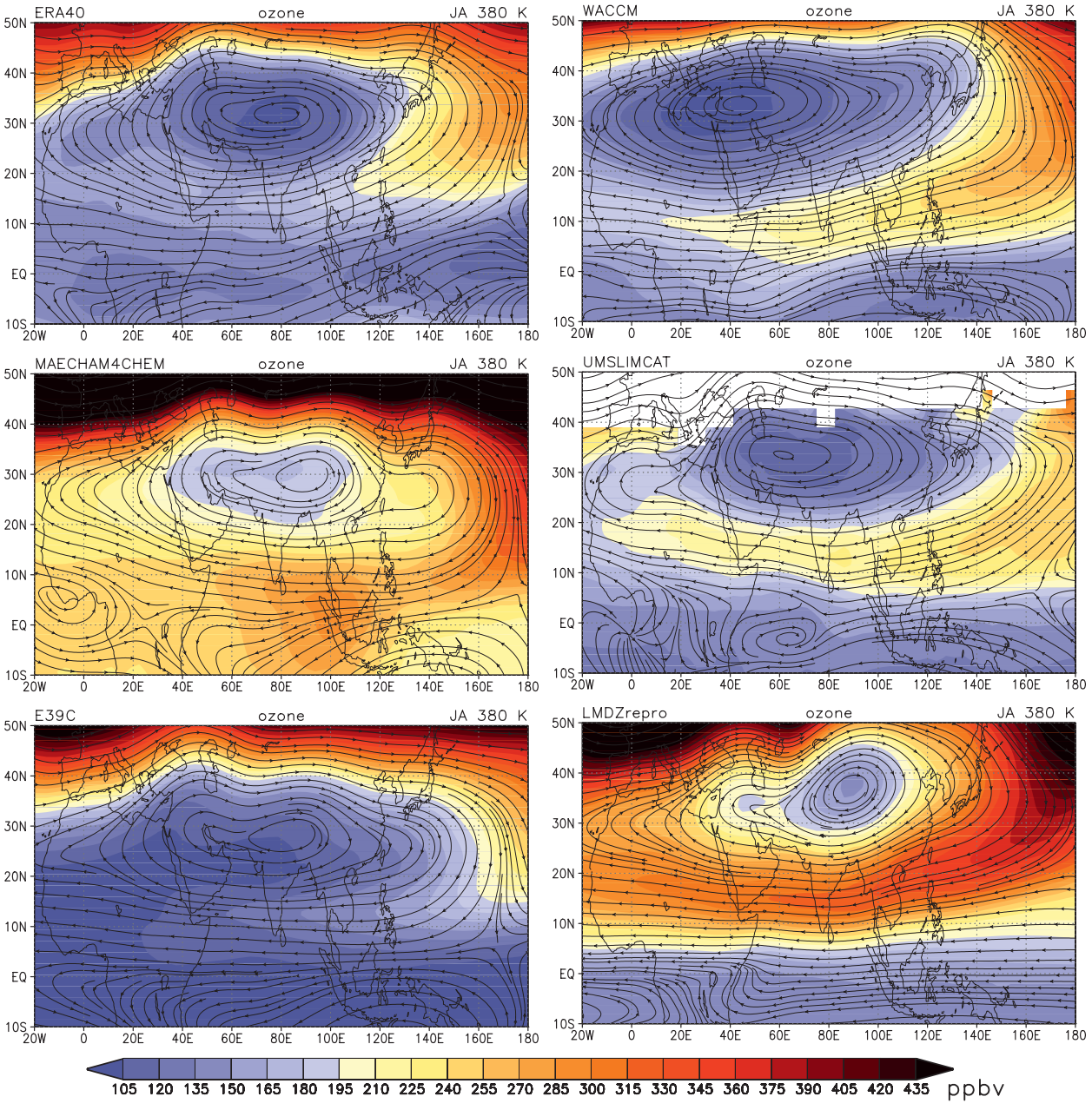

FIG. 6. (*Continued*)

4. Mean monsoon signature in water vapor and ozone

Large dynamical systems like the ISM have implications for tracer distributions in their vicinity. In recent years improvements in earth observation systems allowed the characterization of such tracer anomalies. Gettelman et al. (2004) analyzed water vapor from Halogen Occultation Experiment (HALOE) data at 100 hPa in July and found a clear summer monsoon signal northwest of the Indian subcontinent and over Mexico. Randel and Park (2006) found the strength of the Asian monsoon anticyclone and the tracer variability linked to the occurrence of convection. They found high water vapor concentrations at the 360-K isentropic surface during July–August 2003 coinciding with the monsoon anticyclone. A corresponding decrease in ozone (see also Park et al. 2007) does imply strongly the presence of air of tropospheric origin in the monsoon anticyclone at 360 K.

As an observational reference we use MIPAS satellite data. Figure 5 shows (left) MIPAS water vapor (Milz et al. 2009; von Clarmann et al. 2009) and (right) ozone volume mixing ratios (Steck et al. 2007; von Clarmann et al. 2009) at (top) 360 and (bottom) 380 K averaged over available July and August observations for 2003, 2005, 2006, and 2007. Note that the MHI averaged over this observational period is close to zero and is therefore not affected by a strong/weak ISM. Overlaid streamlines are constructed from ECMWF operational analyses for the corresponding months and years. The MIPAS water vapor measurements at 360 K show a distinct enhancement within the ISM anticyclone with a maximum northeast of the center of the anticyclone. The ozone data at 360 K show a distinct minimum within the ISM anticyclone and also even lower ozone concentrations in the region of the western Pacific warm pool. This is in good agreement with Randel and Park (2006), who analyzed AIRS ozone and water vapor data at 360 K for 2003. Water vapor at 380 K (scale: 4–6 ppmv) shows a clear north–south gradient with enhanced water vapor north of 20°N where the streamfunction indicates the ISM anticyclone. Ozone at 380 K (scale: 105–375 ppbv) in the central region of the ISM anticyclone is low. Enhanced ozone is found to the north and southeast of the central ISM anticyclone. It should be noted that the isolation of tracer concentrations is strongly height and tracer dependent. While at respective pressure or geometric altitude levels the signature of the ISM anticyclone is also clearly visible in the water vapor distributions [similar to Park et al. (2007) and Gettelman et al. (2004)], in the representation at the 380-K isentrope the enhanced levels of water vapor of the ISM anticyclone merge with a band of enhanced water vapor covering all longitudes within Northern Hemisphere midlatitudes, leading to the north–south gradient observed in Fig. 5. At 360 K the water vapor maximum is more pronounced than at 380 K, but the ozone minimum is more pronounced at 380 K compared to 360 K, where the low ozone in the core region of the ISM seems to merge with low tropical ozone. Generally the 380-K isentrope coincides well with the thermal tropopause at equatorial latitudes and lies within the lower stratosphere in high latitudes.

Figure 6 shows modeled water vapor and ozone concentrations at 380 K, together with the streamlines of the horizontal wind fields for ERA-40 and the contributing CCMs. ERA-40 water vapor (scale: 2–20 ppmv, note the extended scale to accommodate all models) shows a north–south gradient and a small enhancement in the center of the ISM anticyclone that is clearly visible in the MIPAS data at 360 K, but not as clear at 380 K. Ozone (scale: 105–435 ppbv, note the extended scale to accommodate all models) shows a very similar behavior in ERA-40 and MIPAS data. In ERA-40 the structures of modeled tracer fields agree well with the dynamical fields. This is not surprising, since the model provides a self-consistent solution to the transport problem. Larger discrepancies between the MIPAS tracers and the ECMWF dynamical fields are evident as the MIPAS observations are independent from the ECMWF analysis system. Additional sampling issues in calculating the averages play a role in explaining some differences between observations and ERA-40. The observed ISM center varies from Pakistan/Afghanistan/the Arabian peninsula in the year 2005 to over northern India in the years 2003 and 2006 to the Tibetan plateau and eastward in the year 2007, smearing out in the multiannual mean. MAECHAM4CHEM shows a distinct water vapor maximum embedded in the strong north–south gradient and a corresponding ozone minimum. The overall ozone gradient is more pronounced than in MIPAS observations and in ERA-40. E39C shows no distinct water vapor maximum and very high water vapor north of 30°N. The ozone distribution in E39C is in good agreement with ERA-40. WACCM shows both a distinct maximum in water vapor and a minimum in ozone. The WACCM modeled ISM center is positioned too far to the west compared to ERA-40. It should be noted that the ECMWF streamfunction corresponding to the MIPAS period (Fig. 5) has its center slightly farther west than the ERA-40 climatological mean for 1980–99. For UMSLIMCAT the chosen level is still close to the lower boundary condition of the stratospheric chemistry module, but both tracer anomalies are present, even though the overall north–south ozone gradient cannot be established. LMDZrepro does not show any distinct water vapor features and the very small ISM center accommodates a dynamical consistent small ozone anomaly.

This comparison reveals weaknesses and strengths in all participating models, and it should be noted that even the observational evidence is not without uncertainties. Generally, it might be acceptable to rate models higher in terms of chemistry–climate interactions that show both tracer anomalies due to the ISM anticyclone (high water vapor/low ozone as in MAECHAM4CHEM, WACCM, and UMSLIMCAT). But this rating is problematic when the position of the ISM anticyclone is taken into account, which is too far to the west in WACCM, surely affecting the climate modeled for the Asian subcontinent.

Figure 4 highlights that the tropopause above the ISM anticyclone (solid red line) is higher than the zonal mean tropopause (dashed red line). The 380-K isentrope (dashed white line) intersects the thermal lapse rate tropopause (30°–40°N). The topography of the 380-K surface as discussed in section 3 is another reason for the

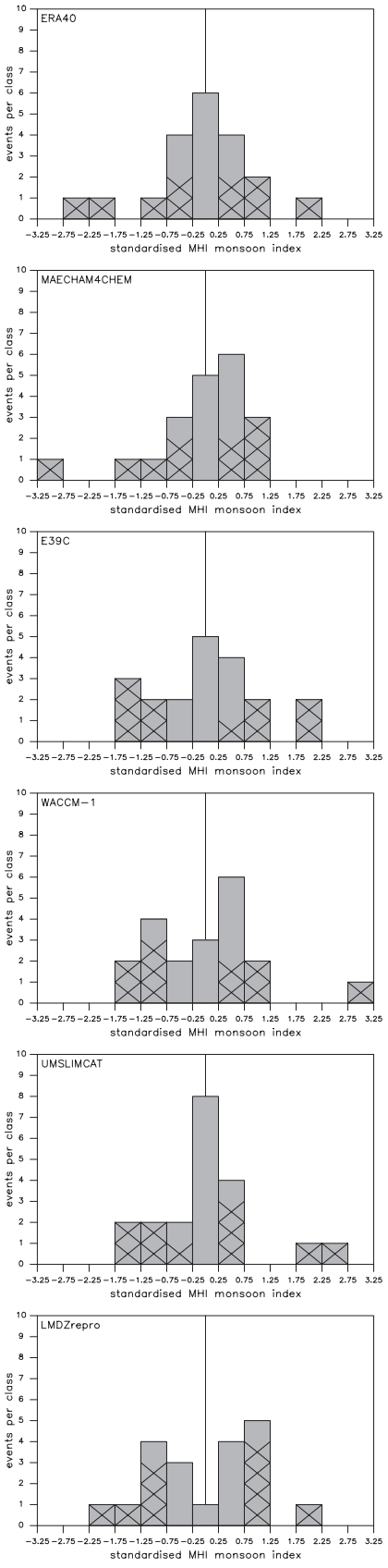

typically higher water vapor and lower ozone concentrations inside the monsoon anticyclone. In addition, vertical exchange processes and the isolation of the ISM anticyclone contribute to the visibility of distinct water vapor and ozone anomalies at certain heights.

5. Interannual monsoon variability

The impact of the ISM anticyclone on the tracer distribution has been assessed in section 4. Here we analyze how the interannual variability of the ISM affects the tracer distribution in the UTLS. We stratify the data according to weak and strong ISM cases identified by the MHI (cf. section 2) and create composite anomalies. Large positive (negative) values of the MHI indicate a strong (weak) northward-directed meridional wind at 850 hPa and a strong (weak) southward-directed meridional wind at 200 hPa. We call these the strong and weak ISM cases, respectively.

Recall that the meteorology of the free-running CCMs is not directly comparable with the ERA-40 reanalysis, even though they all model 1980–99. To create composite differences for strong and weak ISM cases with equal sample size, we sort the years according to the strength of the MHI and use the five years with the lowest and highest MHI values respectively to calculate differences for the July–August period. Given the small number of years (20) and the high variability of the MHI, the differences are not expected to be statistically significant, but as we will demonstrate they reveal some consistent features.

Figure 7 shows the distributions of the MHI for the CCMs and ERA-40 during the July–August period. The distributions are hard to recognize as Gaussian owing to the small number of cases. If at all, a more Gaussian-like distribution can be found for ERA-40 and some of the CCMs (MAECHAM4CHEM, E39C, UMSLIMCAT), whereas LMDZrepro and WACCM show a tendency toward bimodal behavior. Definitely more cases are necessary to draw any further conclusions from Fig. 7, but it documents the variability of the ISM for the CCMs and ERA-40.

Figure 8 shows percentage differences of (left) water vapor and (right) ozone at 380 K for the strong minus weak ISM cases (these cases are marked with crosses in Fig. 7). The differences of the concentrations are shaded.

←

FIG. 7. Histograms of the MHI for the ERA-40 reanalysis and the CCMs. The MHI is calculated for a July–August average. The crosses indicate the five weakest/strongest ISM cases, used to create the composite differences of Fig. 8.

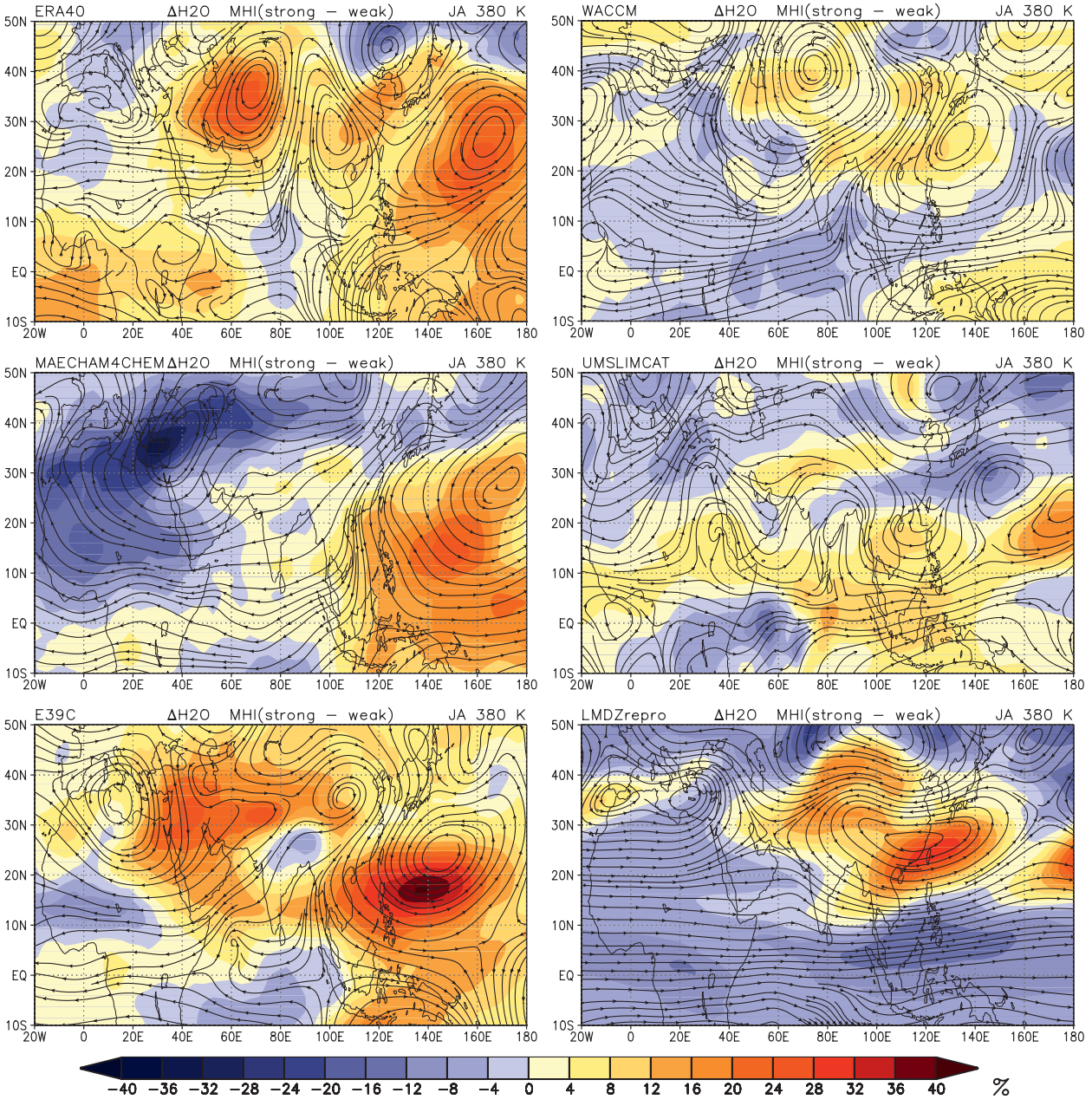

FIG. 8. Composite differences of strong/weak ISM years according to the MHI for a July–August mean. Shading indicates differences of the water vapor mixing ratios in percent: (left page) water vapor; (right page) ozone, Shading interval 4%. Overlaid as streamlines are the differences of the horizontal wind.

Overlaid as streamlines are the differences of the horizontal winds. For ERA-40 we find reduced ozone concentrations in regions of enhanced anticyclonic circulation, indicating strengthened upwelling of ozone-poor air, whereas regions with stronger cyclonic circulation show enhanced ozone concentrations caused by weakened upwelling of ozone-poor air. The ozone anomalies are anticorrelated with water vapor anomalies, suggesting that enhanced transport during strong ISM events is responsible for the anomalies of both constituents. The modeled tracer anomalies in Fig. 8 are fairly different in amplitude and position between the CCMs, but some similar features emerge for both trace gases. WACCM reproduces best the anticorrelation between ozone and water vapor, with a corresponding circulation anomaly around 40°N, 60°E. UMSLIMCAT has only very low amplitude anomalies, quite likely caused by the stratospheric boundary condition of UMSLIMCAT. LMDZrepro shows a very

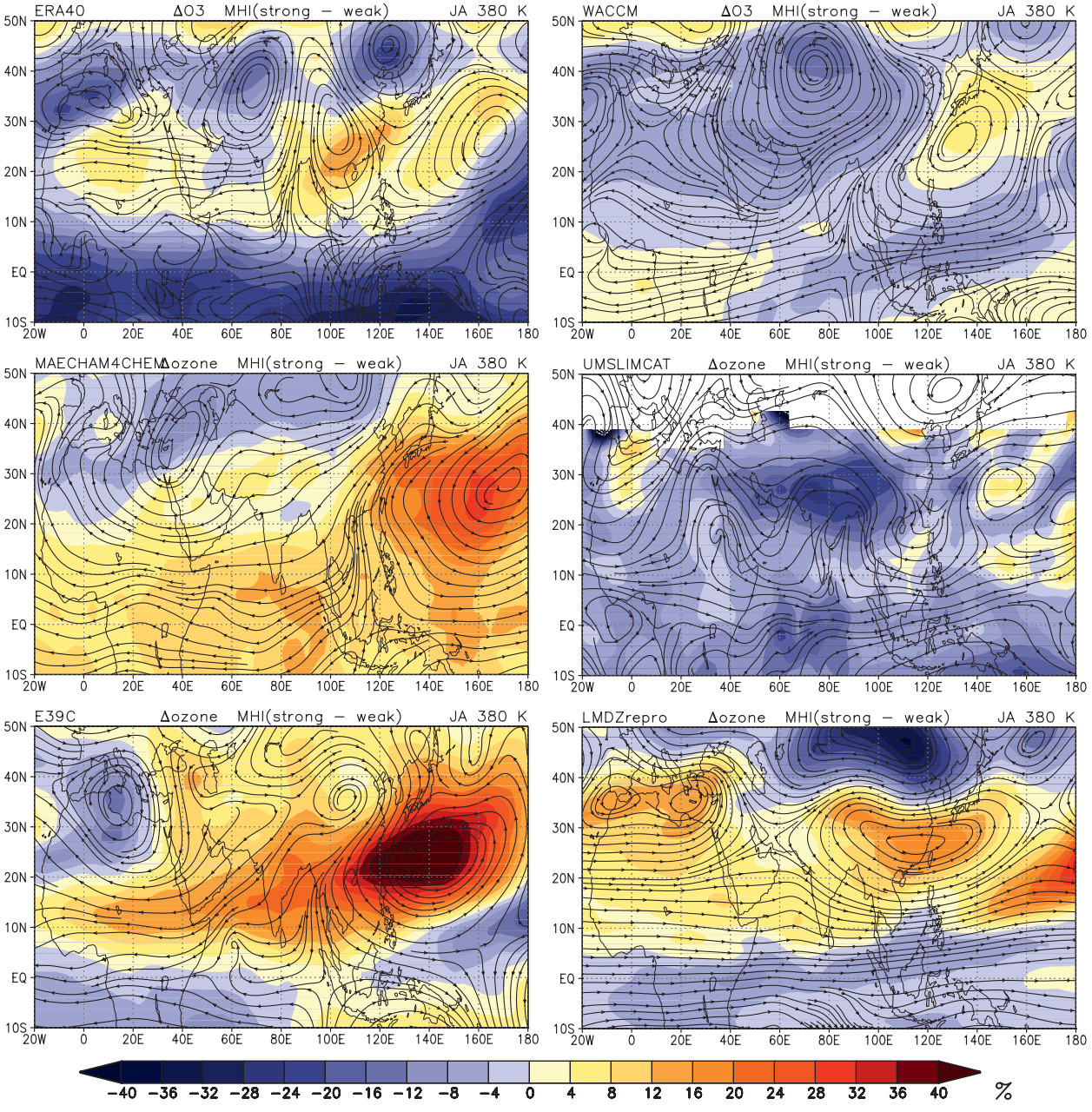

FIG. 8. (*Continued*)

zonal response with only one pronounced north–south dipole. The simplicity of the response hints toward a problem in how this version of the model represents the interannual variability of the ISM anticyclone.

In MAECHAM4CHEM and E39C the circulation anomalies are comparable, as both CCMs are based on the same dynamical model, ECHAM4. However, differences in the tracer anomalies are likely caused by the different transport schemes implemented in the CCMs. According to the analyses of James et al. (2008), we have to assume stronger convection over the Bay of Bengal during stronger ISM cases. This leads to more moist air transported to the TTL where the anticyclonic circulation further transports the air parcels through the TTL toward northwest India, dehydrating at a point warmer than the coldest point of the TTL. As a strong ISM induces a negative temperature anomaly and, thus, a lower cold point, a positive water vapor anomaly in a strong/weak ISM composite difference indicates that the cold point has not been bypassed. On the other hand, a

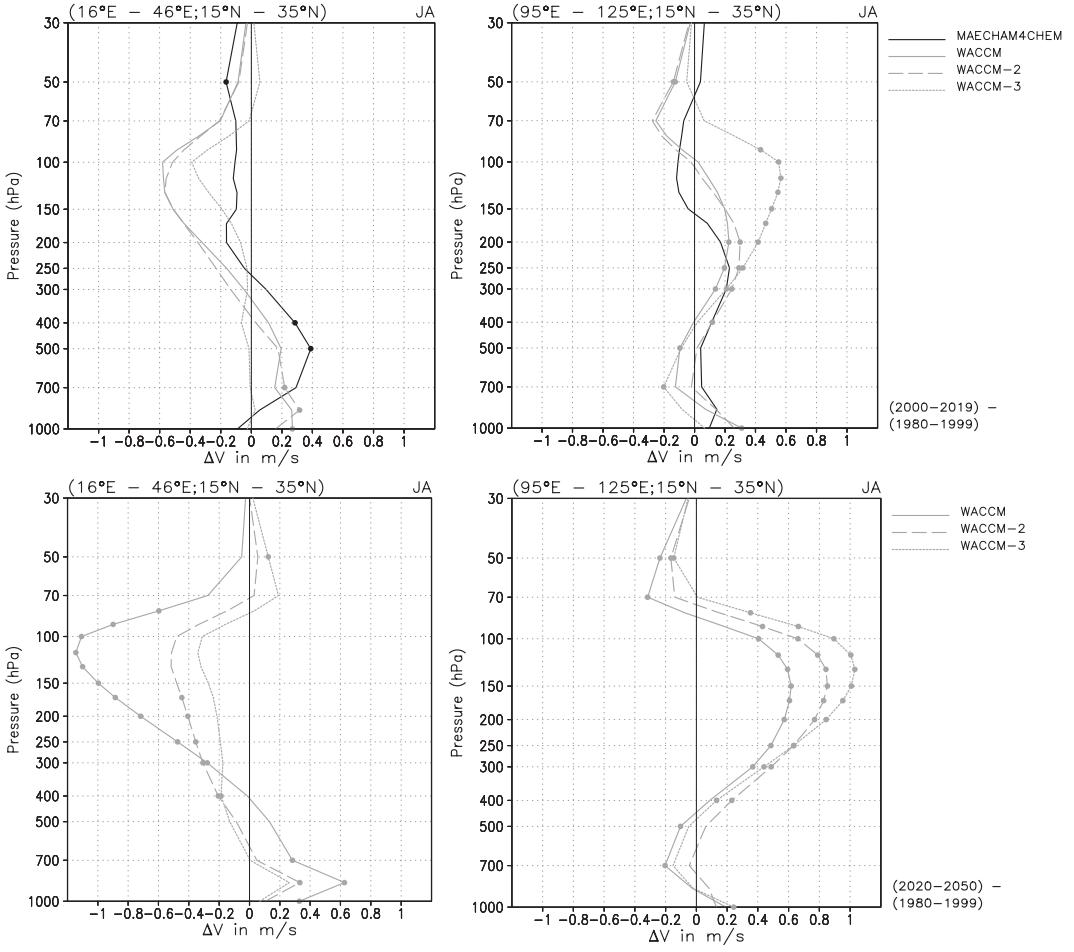

FIG. 9. Vertical profiles of differences of the meridional velocity area averaged for (left) 15°–35°N, 16°–46°E and (right) 15°–35°N, 95°–125°E. Dots mark levels where the differences are statistically significant at the 95% level calculated with a Student's *t* test. (top) Differences between the July and August multiannual mean for 2000–19 minus 1980–99 for MAECHAM4CHEM and WACCM (ensemble of three runs). (bottom) As at top, but for WACCM only and for 2020–50 minus 1980–99.

negative anomaly indicates that the cold point has been bypassed, leading to less water vapor in conjunction with less ozone.

6. Projected monsoon changes and their consequences

Previous studies have assessed potential changes of the ISM in a future climate (e.g., Meehl and Washington 1993; Kitoh et al. 1997; May 2002; Ueda et al. 2006; Kripalani et al. 2007). Doubling the effective CO_2 concentration in a version of the ECHAM4 model (May 2002) leads to an intensification of the monsoon rainfall due to increased moisture transport, while the general monsoon circulation weakens. A similar result is reported by Ueda et al. (2006) from a multimodel analysis of recent coupled atmosphere–ocean GCMs.

Here we will assess indications of future changes of the monsoon circulation in the two CCMs for which data were available, MAECHAM4CHEM and WACCM. Future forcings include anthropogenic and nonanthropogenic boundary conditions as specified for the CCMVal-1 REF2 simulations (Eyring et al. 2005). As an indicator for future circulation changes associated with the ISM, we analyze with Fig. 9 the meridional velocity changes on the eastern and western sides of the ISM anticyclone where the most pronounced meridional flow associated with the ISM anticyclone can be expected between 150 and 100 hPa (northward-directed on the western side and southward-directed on the eastern side of the ISM anticyclone, cf. Fig. 3). Dots mark levels where the differences are statistically significant at the 95% level, calculated with a Student's *t* test.

Figure 9 (top) shows the differences between the regional July and August multiannual means for 2000–19 minus 1980–99 for MAECHAM4CHEM and WACCM (ensemble of three runs). Note that, while the future simulation of MAECHAM4CHEM started in 2000, WACCM started its future climate projections (REF2, cf. section 2) in 1980. We compare here the future changes in WACCM with the 1980–99 period of the REF2 simulations. Unlike for the WACCM REF1 simulation, the position of the ISM anticyclone is well captured in the REF2 simulations, which might be due to differences in the prescribed SSTs in both simulations (cf. Eyring et al. 2005). All three WACCM runs show a decrease of both the (left) northward flow and (right) southward flow peaking between 200 and 100 hPa. Similar changes occur in MAECHAM4CHEM although with smaller amplitude and shifted in height. This weakening of the meridional flow extends down to the lower troposphere where the meridional circulation is reversed (see Fig. 3).

While the future change in the meridional circulation is rather weak and does not show up consistently in all simulations of the near future (2000–19), it is more pronounced for the period 2020–50. The differences in the changes for the ensemble members of WACCM cannot be attributed to a shift in the position of the ISM anticyclone, but reflect the internal model variability. Recall that the monsoon index used for classifying the strength is based on vertical shear in meridional velocities and not on absolute values. Nevertheless, shear and absolute values indicate a weakening of the ISM circulation in a future climate.

Figure 10 shows tracer differences for (left) water vapor and (right) ozone at 380 K between future and recent past time periods. The differences are calculated after removing the zonal average to highlight the ISM impact under climate change. Consequently the changes in ISM signal are less influenced by the model mean state. A Student's *t* test is used to test the significance of the differences at the 95% level (dashed regions). The top row shows percentage differences between the July and August multiannual mean for 2000–19 minus 1980–99 for MAECHAM4CHEM. Contour lines for selected geopotential heights at 150 hPa indicate the position of the ISM anticyclone for the past (1980–99, in black) and the future (in red). It is obvious that the area enclosed by the 1440-gpdm isoline increases in the future. Significant water vapor increases are predicted to the north and the southwest of the anticyclone and in the eastern part of the anticyclone at 360 K (not shown). Ozone increases are more homogeneous with height and ozone is increasing in and around the anticyclone. Consistent changes are simulated in WACCM (Fig. 10, middle) with stronger water vapor increases at 360 K than at 380 K and an improved containment in the ISM anticyclone in WACCM. Ozone at 380 K proves inconclusive with a tendency toward less ozone northwest and southeast of the anticyclone, but lower down some increases are modeled as well. In general these tendencies are confirmed for the extended time horizon from 2020 to 2050 (Fig. 10, bottom). The ozone changes are more pronounced and the areas of significant changes are larger.

The water vapor increase can be related to a relatively lower and warmer tropopause (differences after removing the zonal average; not shown) within the ISM anticyclone. This indicates a weakening of the monsoon circulation, as the ISM usually leads to a higher tropopause (see Fig. 3). The weakening of the ISM is also indicated by the monsoon activity index used, which weakens slightly in a future climate as modeled with WACCM.

Because of the increasing greenhouse gas concentrations prescribed in the model integrations, the troposphere warms in the models and leads to elevated future pressure levels in the upper troposphere; thus, the selected contours of geopotential height at 150 hPa (see Fig. 10) enclose larger areas in the future. This result is consistent with IPCC Fourth Assessment Report (AR4) projections of the future (Meehl et al. 2007, chapter 10), which generally do not consider the stratosphere and chemical processes. The modeled changes of the meridional flow and the change in the MHI indicate a weakening of the ISM circulation. The assessment of the MHI (and other monsoon indices) might be problematic as a sole indicator of ISM strength. The validity of the indices might change in a future climate. Somehow subjective choices for area averages or pressure levels (used in estimating vertical and/or horizontal gradients) might require adaptation in a changing climate.

7. Conclusions

We have presented an assessment of how a group of current CCMs represent the ISM anticyclone in the upper troposphere and lower stratosphere. All models capture some aspects of the mean climatological ISM anticyclone over the period 1980–99. Nevertheless, the strength and position of the ISM anticyclone differ considerably. UMSLIMCAT shows the weakest ISM anticyclone, and the largest (westward) displacement of the center is seen in WACCM, compared to ERA-40 for the period 1980–99.

Modeled tracer concentrations in water vapor and ozone are dynamically consistent in most models, with the exception of water vapor in LMDZrepro. MIPAS observations of water vapor and ozone are in good agreement with ERA-40, but the level of agreement is highly dependent on the exact height of the chosen control level (here 380 K). In agreement with the dynamical

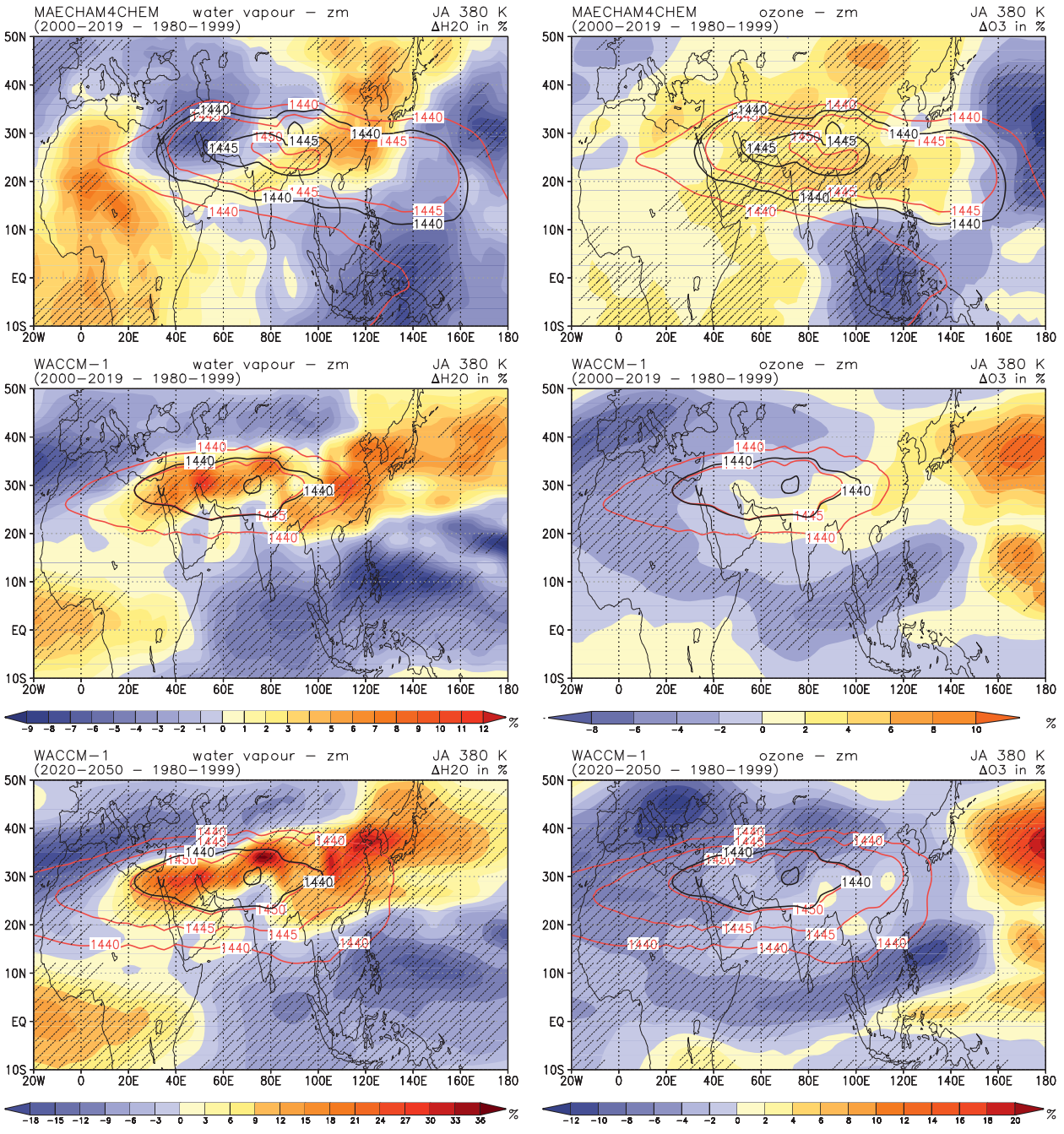

FIG. 10. Tracer differences for (left) water vapor and (right) ozone at 380 K between future and recent past time periods. (top) Percentage differences between the July and August multiannual mean for 2000–19 minus 1980–99 for MAECHAM4CHEM. (middle) As at top but for WACCM. (bottom) As at top but for WACCM and for 2020–50 minus 1980–99. Contour lines for selected geopotential heights at 150 hPa indicate the position of the ISM anticyclone. Black isolines indicate the period 1980–99; red isolines indicate future periods as labeled. In regions with overlaid dashes the results of a Student's *t* test indicate that the differences are statistically significant at the 95% level.

structure of the models, water vapor and ozone anomalies are highly variable, but most models show a clear anticorrelation between the two in the center of the ISM anticyclone (high water vapor/low ozone).

The comparison between weak and strong ISM cases reveals complex dynamical and associated tracer structures. The best agreement for the differences is seen in WACCM at 380 K, even though the mean ISM

anticyclone is too far west in this model. UMSLIMCAT and LMDZrepro show anomalies that do not reflect well the patterns revealed in ERA-40. Our results demonstrate that even for present-day conditions the models do not agree well for extreme events.

In a future climate the models indicate that the used monsoon activity index weakens slightly, which leads to a relative lower and warmer tropopause. Water vapor is predicted to increase in the anticyclone most strongly at 360 K and sometimes above.

The phenomenological nature of this assessment does not provide an objective and unambiguous way of grading the models. From the results presented it is clear that none of the CCMVal-1 models included in this intercomparison captures all aspects of the ISM anticyclone and its imprint on ozone and water vapor in the upper troposphere and lower stratosphere. Nevertheless, it becomes clear from this analysis that some models are better than others in capturing the climatological mean state in comparison to either ERA-40 reanalysis or MIPAS observational data. In addition it is important to note that, even though ERA-40 and MIPAS observational data for water vapor and ozone show clear similarities, they do not agree in all aspects. The complex intersection of characteristic levels (150 hPa, 380 K, and thermal tropopause) is challenging for models and observations alike and poses a challenge that we need to confront continuously.

Further observational data are required to establish the long-term variability of trace gases due to the ISM anticyclone. Given some of the large differences between models and observations regarding the mean position, extent, and interannual variability of the ISM anticyclone it is of paramount importance to scrutinize the reliability of the modeled future changes of the ISM anticyclone. For this study only 20 years could be used to establish the variability of the recent past.

New model experiments within CCMVal-2 will allow a more comprehensive and statistical significant assessment of monsoon variability. Updated model versions are now available. For example, E39C has included a fully Lagrangian advection scheme that leads to a significant improvement of tracer distributions (Stenke et al. 2008) and LMDZrepro has included a new convection parameterization (Hourdin et al. 2006). At the same time ECMWF and NCEP–NCAR will provide new reanalysis products and the satellite observational database will grow continuously. We will aim to reassess soon and will establish the validity of our conclusions.

Acknowledgments. This work has been supported by the European Commission grant through the EC Integrated Project SCOUT-O3 under Contract 505390-GOCE-CT-2004. ESA has provided MIPAS level 1. Parts of this work related to MIPAS has been funded by BMBF under Contract 50-EE-0512. A part of the retrievals was performed on the HP XC4000 of the Scientific Supercomputing Center (SSC) Karlsruhe under Project Grant MIPAS. MAECHAM4CHEM was developed mostly by Benedikt Steil, MPI-C. ECMWF ERA-40 reanalyses used in this study have been obtained from the ECMWF data server. The NCEP–NCAR reanalyses have been downloaded from http://www.cdc.noaa.gov/data/reanalysis/. CCM data have partly been downloaded from the CCMVal data archive at the British Atmospheric Data Centre.

REFERENCES

Annamalai, H., J. Slingo, K. Sperber, and K. Hodges, 1999: The mean evolution and variability of the Asian summer monsoon: Comparison of ECMWF and NCEP/NCAR reanalyses. *Mon. Wea. Rev.,* **127,** 1157–1186.

Bannister, R. N., A. O'Neill, A. R. Gregory, and K. M. Nissen, 2004: The role of the South-east Asian monsoon and other seasonal features in creating the 'tape-recorder' signal in the Unified Model. *Quart. J. Roy. Meteor. Soc.,* **130,** 1531–1554.

Chen, P., 1995: Isentropic cross-tropopause mass exchange in the extratropics. *J. Geophys. Res.,* **100,** 16 661–16 673.

Dameris, M., and Coauthors, 2005: Long-term changes and variability in a transient simulation with a chemistry–climate model employing realistic forcings. *Atmos. Chem. Phys.,* **5,** 2121–2145.

Dessler, A. E., and S. C. Sherwood, 2004: Effect of convection on the summertime extratropical lower stratosphere. *J. Geophys. Res.,* **109,** D23301, doi:10.1029/2004JD005209.

Dethof, A., A. O'Neill, J. M. Slingo, and H. G. J. Smit, 1999: A mechanism for moistening the lower stratosphere involving the Asian summer monsoon. *Quart. J. Roy. Meteor. Soc.,* **125,** 1079–1106.

Dunkerton, T. J., 1995: Evidence of meridional motion in the summer lower stratosphere adjacent to monsoon regions. *J. Geophys. Res.,* **100,** 16 675–16 688.

Eyring, V., D. E. Kinnison, and T. G. Shepherd, 2005: Overview of planned coupled chemistry–climate simulations to support upcoming ozone and climate assessments. *SPARC Newsletter,* No. 25, SPARC International Project Office, Toronto, ON, Canada, 11–17. [Available online at http://www.atmosp.physics.utoronto.ca/SPARC/News25/overview.html.]

——, and Coauthors, 2006: Assessment of temperature, trace species, and ozone in chemistry–climate model simulations of the recent past. *J. Geophys. Res.,* **111,** D22308, doi:10.1029/2006JD007327.

——, and Coauthors, 2007: Multimodel projections of stratospheric ozone in the 21st century. *J. Geophys. Res.,* **112,** D16303, doi:10.1029/2006JD008332.

Fueglistaler, S., and P. H. Haynes, 2005: Control of interannual and longer-term variability of stratospheric water vapor. *J. Geophys. Res.,* **110,** D24108, doi:10.1029/2005JD006019.

Funke, B., and Coauthors, 2009: Carbon monoxide distributions from the upper troposphere to the mesosphere inferred from 4.7 μm non-local thermal equilibrium emissions measured by MIPAS on Envisat. *Atmos. Chem. Phys.,* **9,** 2387–2411.

Garcia, R. R., D. Marsh, D. Kinnison, B. Boville, and F. Sassi, 2007: Simulations of secular trends in the middle atmosphere, 1950–2003. *J. Geophys. Res.,* **112,** D09301, doi:10.1029/2006JD007485.

Gettelman, A., D. E. Kinnison, T. J. Dunkerton, and G. Brasseur, 2004: Impact of monsoon circulations on the upper troposphere

and lower stratosphere. *J. Geophys. Res.,* **109,** D22101, doi:10.1029/2004JD004878.

Goswami, B. N., V. Krishnamurthy, and H. Annamalai, 1999: A broad-scale circulation index for the interannual variability of the Indian summer monsoon. *Quart. J. Roy. Meteor. Soc.,* **125,** 611–633.

Hourdin, F., and Coauthors, 2006: The LMDZ4 general circulation model: Climate performance and sensitivity to parametrized physics with emphasis on tropical convection. *Climate Dyn.,* **27,** 787–813.

James, R., M. Bonazzola, B. Legras, K. Surbled, and S. Fueglistaler, 2008: Water vapor transport and dehydration above convective outflow during Asian monsoon. *Geophys. Res. Lett.,* **35,** L20810, doi:10.1029/2008GL035441.

Jourdain, L., S. Bekki, F. Lott, and F. Lefèvre, 2008: The coupled chemistry–climate model LMDz-REPROBUS: Description and evaluation of a transient simulation of the period 1980–1999. *Ann. Geophys.,* **26,** 1391–1413.

Kalnay, E., and Coauthors, 1996: The NCEP/NCAR 40-Year Reanalysis Project. *Bull. Amer. Meteor. Soc.,* **77,** 437–471.

Kistler, R., and Coauthors, 2001: The NCEP/NCAR 50-Year Reanalysis: Monthly means CD-ROM and documentation. *Bull. Amer. Meteor. Soc.,* **82,** 247–267.

Kitoh, A., S. Yukimoto, A. Noda, and T. Motoi, 1997: Simulated changes in the Asian summer monsoon at times of increased atmospheric CO_2. *J. Meteor. Soc. Japan,* **75,** 1019–1031.

Kripalani, R. H., J. H. Oh, and H. S. Chaudhari, 2007: Response of the East Asian summer monsoon to doubled atmospheric CO_2: Coupled climate model simulations and projections under IPCC AR4. *Theor. Appl. Climatol.,* **87,** 1–28.

Levine, J. G., P. Braesicke, N. R. P. Harris, and J. A. Pyle, 2008: Seasonal and inter-annual variations in troposphere-to-stratosphere transport from the tropical tropopause layer. *Atmos. Chem. Phys.,* **8,** 3689–3703.

Manzini, E., B. Steil, C. Brühl, M. Giorgetta, and K. Krüger, 2003: A new interactive chemistry–climate model. 2: Sensitivity of the middle atmosphere to ozone depletion and increase in greenhouse gases and implications for recent stratospheric cooling. *J. Geophys. Res.,* **108,** 4429, doi:10.1029/2002JD002977.

May, W., 2002: Simulated changes of the Indian summer monsoon under enhanced greenhouse gas conditions in a global time-slice experiment. *Geophys. Res. Lett.,* **29,** 1118, doi:10.1029/2001GL013808.

Meehl, G. A., and W. M. Washington, 1993: South Asian summer monsoon variability in a model with doubled atmospheric carbon dioxide concentration. *Science,* **260,** 1101–1104.

——, and Coauthors, 2007: Global climate projections. *Climate Change 2007: The Physical Science Basis.* S. Solomon et al., Eds., Cambridge University Press, 747–845.

Milz, M., and Coauthors, 2009: Validation of water vapour profiles (version 13) retrieved by the IMK/IAA scientific retrieval processor based on full resolution spectra measured by MIPAS on board Envisat. *Atmos. Meas. Tech. Discuss.,* **2,** 489–559.

Mooley, D. A., and B. Parthasarathy, 1984: Fluctuations in All-India summer monsoon rainfall during 1871–1978. *Climatic Change,* **6,** 287–301.

Mote, W. P., and Coauthors, 1996: An atmospheric tape recorder: The imprint of tropical tropopause temperatures on stratospheric water vapour. *J. Geophys. Res.,* **101,** 3989–4006.

Oikonomou, E. K., and A. O'Neill, 2006: Evaluation of ozone and water vapor fields from the ECMWF reanalysis ERA-40 during 1991–1999 in comparison with UARS satellite and MOZAIC aircraft observations. *J. Geophys. Res.,* **111,** D14109, doi:10.1029/2004JD005341.

Oltmans, S. J., H. Vömel, D. J. Hofmann, K. H. Rosenlof, and D. Kley, 2000: The increase in stratospheric water vapor from balloonborne, frostpoint hygrometer measurements at Washington, D.C. and Boulder, Colorado. *Geophys. Res. Lett.,* **27,** 3453–3456.

Park, M., W. J. Randel, A. Gettelman, S. T. Massie, and J. H. Jiang, 2007: Transport above the Asian summer monsoon anticyclone inferred from Aura Microwave Limb Sounder tracers. *J. Geophys. Res.,* **112,** D16309, doi:10.1029/2006JD008294.

Randel, W. J., and M. Park, 2006: Deep convective influence on the Asian summer monsoon anticyclone and associated tracer variability observed with Atmospheric Infrared Sounder (AIRS). *J. Geophys. Res.,* **111,** D12314, doi:10.1029/2005JD006490.

——, F. Wu, H. Vömel, G. E. Nedoluha, and P. Forster, 2006: Decreases in stratospheric water vapor after 2001: Links to changes in the tropical tropopause and the Brewer–Dobson circulation. *J. Geophys. Res.,* **111,** D12312, doi:10.1029/2005JD006744.

Rosenlof, K. H., and Coauthors, 2001: Stratospheric water vapor increases over the past half-century. *Geophys. Res. Lett.,* **28,** 1195–1198.

Scherer, M., H. Vömel, S. Fueglistaler, S. J. Oltmans, and J. Staehelin, 2008: Trends and variability of midlatitude stratospheric water vapour deduced from the re-evaluated Boulder balloon series and HALOE. *Atmos. Chem. Phys.,* **8,** 1391–1402.

Shine, K. P., and P. M. Forster, 1999: The effect of human activity on radiative forcing of climate change: a review of recent developments. *Global Planet. Change,* **20,** 205–225.

Steck, T., and Coauthors, 2007: Bias determination and precision validation of ozone profiles from MIPAS-Envisat retrieved with the IMK-IAA processor. *Atmos. Chem. Phys.,* **7,** 3639–3662.

Steil, B., C. Brühl, E. Manzini, P. J. Crutzen, J. Lelieveld, P. J. Rasch, E. Roeckner, and K. Krüger, 2003: A new interactive chemistry–climate model: 1. Present-day climatology and interannual variability of the middle atmosphere using the model and 9 years of HALOE/UARS data. *J. Geophys. Res.,* **108,** 4290, doi:10.1029/2002JD002971.

Stenke, A., V. Grewe, and M. Ponater, 2008: Lagrangian transport of water vapor and cloud water in the ECHAM4 GCM and its impact on the cold bias. *Climate Dyn.,* **31,** 491–506.

Tian, W., and M. P. Chipperfield, 2005: A new coupled chemistry–climate model for the stratosphere: The importance of coupling for future O_3–climate predictions. *Quart. J. Roy. Meteor. Soc.,* **131,** 281–303.

Ueda, H., A. Iwai, K. Kuwako, and M. E. Hori, 2006: Impact of anthropogenic forcing on the Asian summer monsoon as simulated by eight GCMs. *Geophys. Res. Lett.,* **33,** L06703, doi:10.1029/2005GL025336.

Uppala, S. M., and Coauthors, 2005: The ERA-40 re-analysis. *Quart. J. Roy. Meteor. Soc.,* **131,** 2961–3012.

von Clarmann, T., and Coauthors, 2003: Retrieval of temperature and tangent altitude pointing from limb emission spectra recorded from space by the Michelson Interferometer for Passive Atmospheric Sounding (MIPAS). *J. Geophys. Res.,* **108,** 4736, doi:10.1029/2003JD003602.

——, and Coauthors, 2009: Retrieval of temperature, H_2O, O_3, HNO_3, CH_4, N_2O, $ClONO_2$ and ClO from MIPAS reduced resolution nominal mode limb emission measurements. *Atmos. Meas. Tech.,* **2,** 159–175. [Available online at http://www.atmos-meas-tech.net/2/159/2009/.]

WMO, 2003: *Scientific Assessment of Ozone Depletion: 2002*. Global Ozone Research Monitoring Project Rep. 47, 498 pp.

——, 2007: *Scientific Assessment of Ozone Depletion: 2006*. Ozone Research Monitoring Project Rep. 50, 572 pp.